HEALTH AND MEDICINE

Raman spectroscopy imaging reveals interplay between atherosclerosis and medial calcification in the human aorta

Amanda Y. F. You,[1,2,3] Mads S. Bergholt,[1,2,3] Jean-Philippe St-Pierre,[1,2,3]* Worrapong Kit-Anan,[1,2,3] Isaac J. Pence,[1,2,3] Adrian H. Chester,[4] Magdi H. Yacoub,[4] Sergio Bertazzo,[5] Molly M. Stevens[1,2,3]†

Medial calcification in the human aorta accumulates during aging and is known to be aggravated in several diseases. Atherosclerosis, another major cause of cardiovascular calcification, shares some common aggravators. However, the mechanisms of cardiovascular calcification remain poorly understood. To elucidate the relationship between medial aortic calcification and atherosclerosis, we characterized the cross-sectional distributions of the predominant minerals in aortic tissue, apatite and whitlockite, and the associated extracellular matrix. We also compared the cellular changes between atherosclerotic and nonatherosclerotic human aortic tissues. This was achieved through the development of Raman spectroscopy imaging methods that adapted algorithms to distinguish between the major biomolecules present within these tissues. We present a relationship between apatite, cholesterol, and triglyceride in atherosclerosis, with the relative amount of all molecules concurrently increased in the atherosclerotic plaque. Further, the increase in apatite was disproportionately large in relation to whitlockite in the aortic media directly underlying a plaque, indicating that apatite is more pathologically significant in atherosclerosis-aggravated medial calcification. We also discovered a reduction of β-carotene in the whole aortic intima, including a plaque in atherosclerotic aortic tissues compared to nonatherosclerotic tissues. This unprecedented biomolecular characterization of the aortic tissue furthers our understanding of pathological and physiological cardiovascular calcification events in humans.

INTRODUCTION

Cardiovascular diseases represent the most common cause of global mortality (31%), affecting both developed and developing countries, claiming the lives of an estimated 17.5 million people in 2012 (*1*–*3*). Among the predictors for cardiovascular morbidity and mortality, cardiovascular calcification is an independent risk factor. Many pathologies, such as atherosclerosis, diabetes mellitus, and chronic kidney disease, are often associated with cardiovascular calcification (*4*, *5*), which can occur in blood vessels, the myocardium, and cardiac valves. In blood vessels, calcification typically occurs in intimal atherosclerotic plaques and in the tunica media (*4*, *6*–*8*).

In the past two decades, research has highlighted the active inflammatory and/or osteogenic signaling processes that contribute to pathological cardiovascular calcification, shifting the paradigm away from that of a passive accumulation of minerals (*9*, *10*). However, very little is known about the mechanism of nonpathological mineral accumulation in the aortic media with age (*11*–*13*). In 2013, Bertazzo *et al.* (*14*) reported that spherical particles of highly crystalline hydroxyapatite were detected as a very early form of calcification in cardiovascular tissues. In vitro studies have also identified hydroxyapatite as the mineral phase in vascular calcification, with amorphous calcium phosphate precursors (*15*, *16*). These findings emphasized the need to delineate molecular complexity given that there could be multiple mechanisms at play at any one time. In general, two types of mineral, apatite and whitlockite, predominate in studies of cardiovascular tissue. Nonstoichiometric, carbonated apatite is the form of calcium phosphate most commonly found in the human body, whereas whitlockite has been reported to be a magnesium-substituted calcium phosphate $(Ca,Mg)_3(PO_4)_2$ (*11*, *17*).

Atherosclerosis presents itself in the intima of arteries via the accumulation of focal intimal plaques, consisting mainly of lipoproteins, oxidized lipoproteins, cellular debris, inflammatory cells, and, finally, deposits of apatite (*18*). Macrophages have been inferred to mediate the calcification process linked with this pathology (*19*), which changes the mechanical properties of the plaque and leads to an increased risk of microfractures that can cause plaque rupture (*20*–*23*). Whereas atherosclerotic plaques can restrict blood flow, clots formed by the release of rupture debris can lead to stroke or myocardial infarction by traveling further along the vascular system, causing the blockage in narrower arteries (*24*).

In contrast, medial artery calcification in the tunica media of large arteries is typically composed of both apatite and whitlockite crystals (*11*). A number of studies have associated medial minerals with elastin fibers, whereas plaque calcification is embedded within lipid deposits (*25*–*27*). The presence of calcification in the media has been linked with increased stiffness in severely affected arteries and associated with isolated systolic hypertension (*28*). Although most in vitro and in vivo studies to date have focused on the later stages of medial calcification, the earliest signs of disease are yet to be identified.

Medial calcification has been reported to increase with both age (*11*, *13*) and diseases such as diabetes mellitus and chronic kidney disease (*29*). Diabetes has been reported to not only increase medial calcification (*6*, *29*) but also accelerate atherosclerosis (*30*, *31*). Thus far, studies of atherosclerosis have used tools that are limited in spatial resolution, preventing the observation of early stages of media calcification.

[1]Department of Materials, Imperial College London, London SW7 2AZ, UK. [2]Department of Bioengineering, Imperial College London, London SW7 2AZ, UK. [3]Institute of Biomedical Engineering, Imperial College London, London SW7 2AZ, UK. [4]National Heart and Lung Institute, Harefield Heart Science Centre, Imperial College London, Harefield, Middlesex UB9 6JH, UK. [5]Department of Medical Physics and Biomedical Engineering, University College London, Malet Place Engineering Building, London WC1E 6BT, UK.
*Present address: Department of Chemical and Biological Engineering, University of Ottawa, Ottawa K1N 6N5, Canada.
†Corresponding author. Email: m.stevens@imperial.ac.uk

This also raises the question of what happens when medial calcification is increased, and whether the mineral species in the aortic media are similar to those in atherosclerotic plaques and accompanied by concomitant increases in plaque-associated lipids in the aortic media.

Traditional analytical methods used to visualize atherosclerosis, such as histology and immunohistochemistry, are labor-intensive and inherently semiquantitative. Electron microscopy (EM) has also been applied to study atherosclerotic calcification (*32*). Although EM provides highly spatially resolved images and can be combined with energy-dispersive x-ray spectroscopy (EDS) and selected-area electron diffraction to provide elemental and crystal structure information, EM and EDS together do not provide complementary molecular information on the surrounding organic tissue or quantitative information of the mineral phase.

Raman spectroscopy is an inelastic light scattering technique that provides the biomolecular information of extra- and intracellular constituents (for example, minerals, lipids, proteins, etc.) with submicrometer resolution. It has been used to show the distribution of different proteins, lipids, and mineral species in a number of tissues (*33*, *34*). Multivariate analysis and spectral unmixing methods can be used to resolve the information collected and aid in the unbiased analysis of the large data sets from these experiments (*35*).

Raman spectroscopy has previously been used in the en face characterization of the atherosclerotic plaque (*36*–*46*). Latterman *et al.* (*47*) imaged the cross section of atherosclerotic plaques from rabbits with high-cholesterol diet–induced disease using Raman and Fourier transform infrared spectroscopy and provided a detailed characterization of the lipidic components in the tissues. Other groups have developed fiber-optic techniques using miniaturized Raman probes to aid in the diagnosis of atherosclerosis in vivo (*36*, *45*).

It is clear that Raman spectroscopy has the potential to further our understanding of cardiovascular calcification. There is an important need to thoroughly characterize and compare the spatial distribution of biochemical components throughout the depth of healthy and diseased aortic tissues.

Here, we use Raman spectroscopy imaging to examine the composition and spatial distribution of mineral and organic content in human aortic tissue cross sections. We compared atherosclerotic tissues to age-matched healthy tissues. We also evaluated the difference between the young and old age groups (below and above the age of 50, respectively). By developing a comprehensive multivariate model based on spectral unmixing, we quantified the relative biochemical distributions across the depth of aortic tissues.

We hypothesized that the accumulation of minerals in age-related medial calcification and atherosclerosis is the result of different fundamental mechanisms as manifested by mineral species. The results of this study present a new and comprehensive characterization of the human aorta in healthy versus diseased tissues and young versus old age.

RESULTS

Raman spectroscopy imaging reveals a biochemical distribution in the aorta

Raman spectroscopy imaging of the entire aortic cross section was performed on a total of 41 tissues from 31 donors. This included atherosclerotic samples in areas including a plaque (Ath_p) (n = 10 donors), atherosclerotic samples adjacent to plaque areas (Ath_{np}) (n = 12 donors), nonatherosclerotic samples from donors older than 50 years of age ($NAth_{>50}$) (n = 9 donors), and nonatherosclerotic samples from donors younger than 50 years of age ($NAth_{<50}$) (n = 10 donors) (see Table 1 for details of the samples). In Fig. 1, we present the Raman spectroscopic image of a nonatherosclerotic aorta cross section from the intima to the adventitia, in which we identified representative spectra rich in specific components of the aortic tissue, including elastin, collagen, lipid (cholesterol), β-carotene, apatite, and whitlockite (Fig. 1A).

Characteristic marker bands in the Raman spectra for proteins were observed at 1003, 1031, 1258, 1450, and 1665 cm^{-1}, which correspond to phenylalanine, amide III, CH_2 and CH_3 deformations, and amide I, respectively (*48*). Besides markers for protein in general, elastin demonstrates distinctive bands of its unique amino acids desmosine and isodesmosine, which were observed at 527 and 1105 cm^{-1}, respectively (*48*). Characteristic collagen proline and hydroxyproline bands were also observed at 855 and 877 cm^{-1}, respectively (*49*).

The cholesterol and cholesterol ester lipids were identified successfully using a specific peak at 701 cm^{-1} that arises from the steroid ring vibration of both types of biomolecules (*48*). The CH_2 and CH_3 deformations of lipids at 1440 cm^{-1} were also identifiable and were slightly offset from those of proteins. β-Carotene, which shows an inherently strong Raman scattering, was easily identified with its strong Raman bands at 1157 and 1526 cm^{-1} (*36*).

Two mineral species, apatite and whitlockite, were identified in the aortic cross section and were detected via their known phosphate bands. These phosphate ν_1 stretching bands appeared at 960 cm^{-1} for apatite and 970 cm^{-1} for whitlockite. The position of whitlockite phosphate ν_1 has been reported on biological, geological, and synthetic whitlockite (*50*–*52*).

These characteristic bands were used to image the distribution of elastin, collagen, lipid, β-carotene, apatite, and whitlockite (Fig. 1B). These cross-sectional images provide an appreciation for the overall structure of the aorta based on biochemical landmarks. We also collected high-resolution Raman spectroscopy images (spatial resolution of 0.8 μm) to visualize the spatial distribution of the various components in greater detail (Fig. 1, C and D). These images depicted the elongated strands of elastin fibers with interspersed mineral (predominantly whitlockite) and collagen in the media. These maps also demonstrated the different distribution patterns of whitlockite and apatite through the cross section of the aorta.

Relative whitlockite levels in the aortic media increase with age, whereas apatite levels are increased in atherosclerosis

Two mineral types, whitlockite and apatite, were observed in all aortic samples tested. To evaluate their relative distribution, we plotted the average ratios of whitlockite to total mineral (apatite + whitlockite) in the intima/plaque and media regions (Fig. 2). When comparing levels between the intima and the media, whitlockite was predominantly present in the aortic media ($P < 0.01$), whereas apatite is mainly present in the aortic intima/plaque ($P < 0.05$), especially for the $NAth_{<50}$ and Ath_p groups (fig. S1). Figure 2 highlights a decrease in whitlockite ratio for the Ath_p group in the media compared to both the Ath_{np} and the $NAth_{>50}$ groups ($P < 0.01$). Intriguingly, the $NAth_{>50}$ and Ath_{np} groups showed significantly higher whitlockite ratios in the media compared to the $NAth_{<50}$ group ($P < 0.01$) and no difference in the intima (Fig. 2). These results indicate that there is a significant increase of whitlockite relative to apatite in the aortic media with age, which is reversed by the presence of atherosclerotic plaque in the directly underlying media.

Spectral unmixing reveals nine different major biochemical components

To separate the Raman spectra of specific biochemical components that contain overlapping peaks and thereby reliably characterize their

Table 1. Experimental groups and donor information.

Experimental groups	Abbreviation	Donors	Tissue samples	Age range	Average age	Male/female ratio
Nonatherosclerotic, <50 years	$NAth_{<50}$	10	13	14–39	27	0.67
Nonatherosclerotic, >50 years	$NAth_{>50}$	9	12	54–65	58	1.25
Atherosclerotic nonplaque, >50 years	Ath_{np}	12	15	57–64	57	0.50
Atherosclerotic plaque, >50 years	Ath_{p}	10	13	57–65	57	0.43

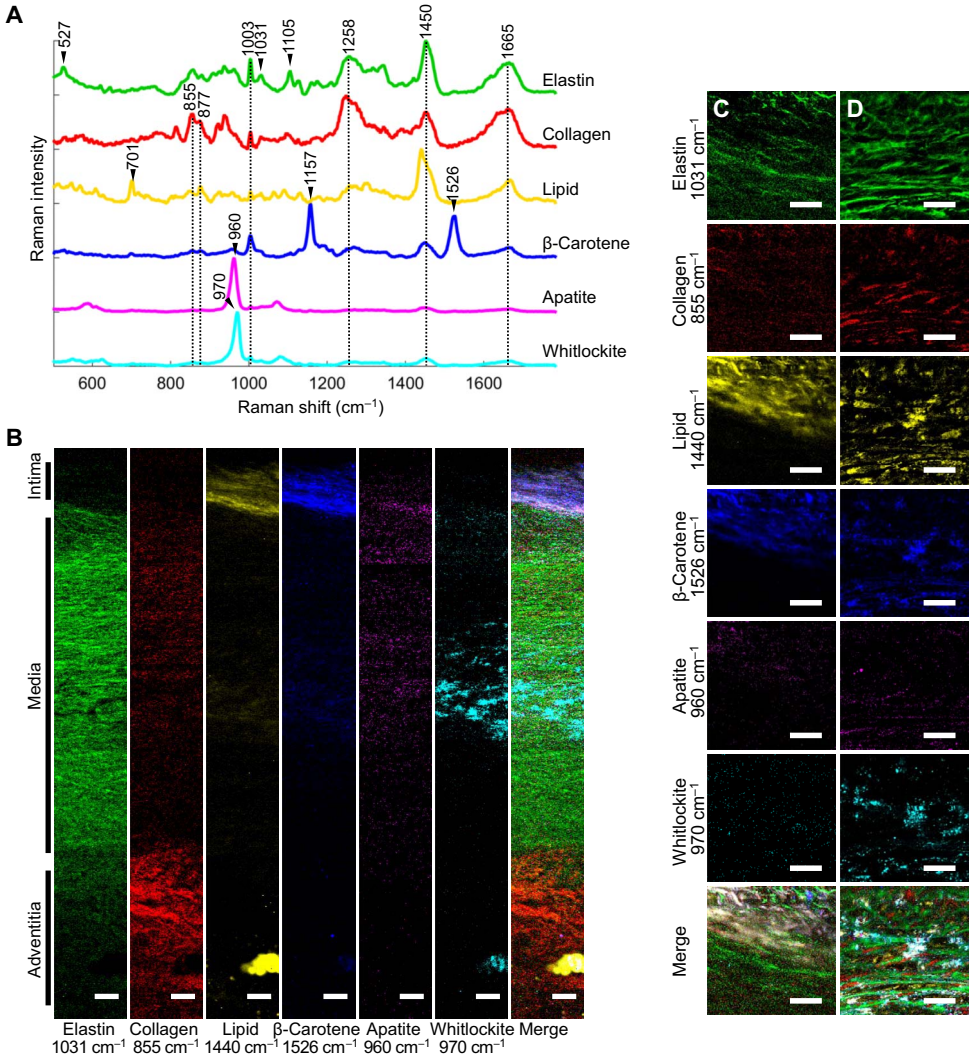

Fig. 1. Univariate Raman spectroscopy images of the cross section of a representative nonatherosclerotic aorta (65 years old). (**A**) Representative spectra rich in specific aortic components. (**B**) Univariate heat maps of the entire cross section of a nonatherosclerotic aorta were plotted according to the signature peaks listed. (**C** and **D**) High-resolution maps at the intima-media interface (C) and within the media (D) were also plotted. Merge refers to a composite image of all the univariate heat maps. Scale bars, 100 μm (B) and 50 μm (C and D).

distributions, we next performed pure spectral unmixing of the data using vertex component analysis (VCA) (Fig. 3, A and B, and fig. S2). We successfully extracted nine main components as endmembers: collagen, elastin, actin, cholesterol ester, cholesterol, triglycerides, β-carotene, whitlockite-rich, and apatite-rich (Fig. 3A). Where pure chemicals were available, endmember spectra were validated by comparing to laboratory-grade commercial biochemical powders (fig. S3). The R^2 values showed good correlations for β-carotene (R^2 = 0.74), cholesterol (R^2 = 0.72), cholesterol ester (R^2 = 0.94), triglyceride (R^2 = 0.86), elastin (R^2 = 0.98), collagen (R^2 = 0.90), and actin (R^2 = 0.94). The pure hydroxyapatite spectrum shown in fig. S3 had a low R^2 value (R^2 = 0.11) against the apatite-rich VCA endmember spectrum in Fig. 3. This is because the

endmember spectrum contained some signal from organic components and is not pure apatite. Nevertheless, the apatite endmember spectrum showed a distinct peak at 960 cm^{-1} that is a clear indication of hydroxyapatite. Synthetic whitlockite is not commercially available for comparison. However, in studies of dentin and in geological, synthetic, and biological samples, the phosphate ν_1 peak at 970 cm^{-1} has been reported as whitlockite (*51*, *52*).

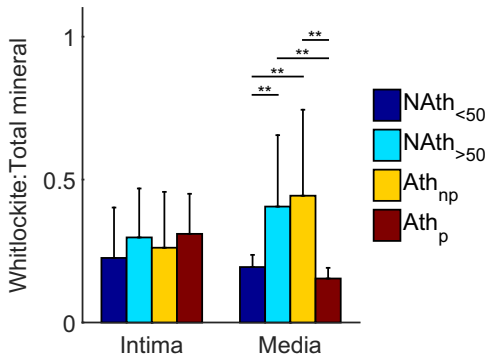

Fig. 2. Ratio of whitlockite to total mineral (apatite + whitlockite) from univariate quantification of the phosphate ν_1 peak. Average ratios of whitlockite over total mineral within the intima and media. Statistical significance was defined using generalized linear model (GLM) regression followed by analysis of variance (ANOVA); error bars denote 95% confidence intervals. $^{**}P < 0.01$, $n \geq 9$ donors per group.

To generate representative images for each experimental group, we next calculated the relative concentrations of biochemicals relating to each endmember for each spectrum using nonnegative least-squares regression (Fig. 3B). The major extracellular matrix components of the media (elastin) and the adventitia (collagen) were observed in their proper spatial arrangements and confirmed with Verhoeff trichrome and picrosirius red histology stainings. Actin-rich cell spectra were also distinguishable across the tissues and concentrated in the media. This observation was corroborated by Verhoeff trichrome staining, DAPI, and α-SMA immunofluorescence. Cholesterol ester was observed in the intima of all experimental groups, whereas triglyceride and cholesterol lipid droplets of around 10 μm in diameter were only observed in the intima/plaque areas of atherosclerotic tissues. High amounts of triglyceride were only occasionally observed in certain areas of the aortic adventitia. Nile red images corroborated the high lipidic content of the plaque and the comparatively low lipidic content in the aortic cross section of nonatherosclerotic samples. Macrophage marker CD68 highlighted the presence of macrophages in the atherosclerotic plaque and sporadically in the aortic media of donors above 50 years of age (Fig. 3B). Low amounts of β-carotene were observed in the intima. Because of its sparse distribution, β-carotene could not be visualized clearly in whole cross-sectional images. Apatite and whitlockite were found in

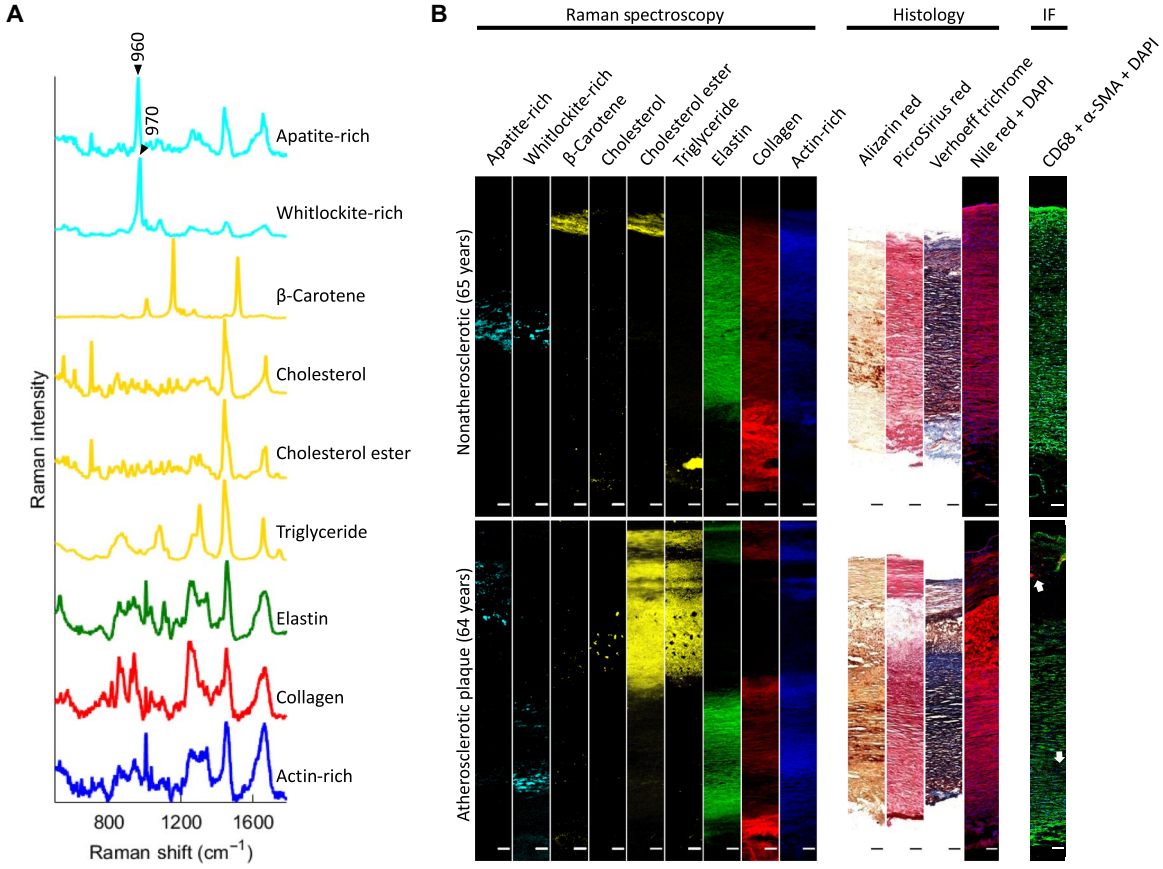

Fig. 3. VCA on Raman spectroscopy images and relevant histology images. (**A**) VCA endmember spectra for nine major components of aortic tissues were found. (**B**) Representative VCA images, associated histology, and immunofluorescence [red, CD68; green, α–smooth muscle actin (α-SMA); blue, 4′,6-diamidino-2-phenylindole (DAPI)] of aortic tissues from a nonatherosclerotic 65-year-old donor and an atherosclerotic 64-year-old donor (tissue sample taken from the plaque region). Arrows indicate CD68-positive areas. Scale bars, 100 μm. IF, immunofluorescence.

all experimental groups above 50 years of age. Whitlockite was localized primarily in the media, whereas apatite was observed in both the media and the atherosclerotic plaque. Alizarin red S histology images were in agreement with the Raman results on mineral content. Together, these results showed that Raman spectroscopy and spectral unmixing could be used to achieve an unprecedented biomolecular characterization of healthy and diseased aortic tissues.

Apatite, cholesterol, cholesterol ester, and triglyceride levels concurrently increase in atherosclerosis

Next, we plotted the depth distribution profiles for the relative quantity of each endmember component, ranging from the intima to the media-adventitia interface (Fig. 4A and fig. S4A). To obtain zone-specific information in the intima (or plaque for the atherosclerotic plaque experimental group) and media, we chose the border between cholesterol ester and elastin to separate each Raman image (Fig. 4B and fig. S4B). In the $NAth_{>50}$ and Ath_{np} groups, apatite and whitlockite depth profiles were very similar. We found significantly increased apatite ($P < 0.01$) in the atherosclerotic plaque compared to the intima for all other experimental groups. In the aortic media, the relative concentration of whitlockite was significantly increased in the Ath_p group compared to both nonatherosclerotic experimental groups ($P < 0.05$). These results indicated that in atherosclerosis, mineral changes occur mainly in the underlying tissue area, whereby apatite content increases in the plaque and whitlockite content increases in the aortic media.

In atherosclerotic plaques, the increase of apatite, cholesterol, and triglyceride levels is at least five times higher in the Ath_p group compared to the intima of all other groups ($P < 0.01$) (Fig. 4). However, cholesterol ester was only increased slightly in the plaque of the Ath_p group compared to the intima of the Ath_{np} group. No significant difference was observed in these lipidic compounds between the $NAth_{<50}$ and $NAth_{>50}$ groups. Our results indicate that relative cholesterol ester, cholesterol, and triglyceride contents were only locally increased in the atherosclerotic plaque. Cholesterol ester has a different depth profile as compared to the more similar apatite, cholesterol, and triglyceride, indicating that it is also normally present in healthy aortic intima (Fig. 4).

β-Carotene levels are decreased throughout the entire atherosclerotic intima

We observed β-carotene to be preferentially located in the intima of all samples examined (fig. S4). In both atherosclerotic experimental groups, only low amounts of β-carotene were observed in the intima compared to the $NAth_{<50}$ group ($P < 0.05$). Between the nonatherosclerotic samples, the β-carotene levels of the $NAth_{<50}$ group were similar to those of the older $NAth_{>50}$ group. In the media, no significant difference was observed. These results suggest that atherosclerosis correlates with an overall reduction in β-carotene levels in the aortic intima.

Other differences in organic content

Significant changes in protein components between the groups were also found. Ath_{np} group showed higher relative elastin ($P < 0.05$) and actin ($P < 0.01$) levels compared to the Ath_p group in the plaque/intima region (fig. S4). Relative collagen levels indicated a reduction of collagen with age in the intima. These results suggested that the relative collagen levels were not affected by atherosclerosis, whereas relative concentrations of actin-rich cells and elastin decreased in the atherosclerotic plaque. Comparisons of nonplaque and plaque regions confirm the significant differences for each component within the same donor (fig. S5).

DISCUSSION

Delineation of apatite and whitlockite cross-sectional distribution

The aim of our study was to identify the changes occurring in aortic tissues during atherosclerosis and aging by evaluating tissues classified as atherosclerotic or nonatherosclerotic from age-matched individuals and from younger individuals. Our results highlighted important differences in the accumulation of two mineral phases, apatite and whitlockite, and in the distribution of the major matrix components, β-carotene, and lipidic compounds between these different groups.

Medial calcification is locally increased in atherosclerosis

Apatite and whitlockite are the two mineral phases that have been associated with aortic tissue (*11*, *17*). Apatite is generally associated with atherosclerotic plaques and arteriosclerosis in the tunica media, resulting in hardening of the aorta (*6*, *53*). In addition, whitlockite (and apatite) nano- and microscale particles have been observed in healthy human aortic tissue with increasing age-related concentration (*11*, *13*). It is common to observe high amounts of medial calcification in aged individuals but in the absence of other diseases, as shown in previous literatures (*11*–*13*). The cause of this calcification is still unknown. Our findings revealed a more intricate landscape with both apatite and whitlockite spectra present in the intima and the tunica media, albeit at varying concentrations.

Age-related nonatherosclerotic medial calcification consists of whitlockite and apatite. However, the aortic media directly underlying an atherosclerotic plaque has a ratio of apatite to whitlockite similar to that of the aortic intima and plaque, with apatite being the predominating mineral species.

Our results indicate that in the event of atherosclerosis, a local change in the tissue environment is elicited that promotes the disproportionate accumulation of apatite within the atherosclerotic plaque and the directly underlying media. This local phenomenon does not change the whitlockite-to-apatite ratios in the rest of the tissue, although it affects the aortic media directly underlying the plaque in a more complex way, increasing whitlockite and apatite levels.

This increase in medial calcification in the atherosclerotic plaque experimental group suggested that there is a complex relationship between atherosclerosis and medial calcification, although the precise nature of this relationship remains unresolved. Considering the increase in apatite relative to whitlockite in the aortic media directly underlying plaque regions, this indicates that atherosclerosis aggravates medial calcification by whitlockite accumulation (similar to aging) and offsetting the ratio between apatite and whitlockite (similar to the plaque region). Medial invasion of the atheroma has been reported in a previous literature; however, this does not address the increase in whitlockite levels (*54*). Furthermore, diseases such as diabetes mellitus have been associated with medial calcification and the aggravation of atherosclerosis (*29*, *55*–*58*). The evaluation of aortic samples from diabetic patients may provide insight into the mechanism by which this relationship develops.

Cholesterol and triglyceride show similar cross-sectional distribution to apatite

As predicted, we observed a much higher relative lipid content spread over a larger area in the atherosclerotic plaque group compared to all other groups. Specifically, we found increases in both cholesterol and cholesterol ester in the plaque region compared to the intima of all other groups, which is in agreement with previous gas chromatography–mass

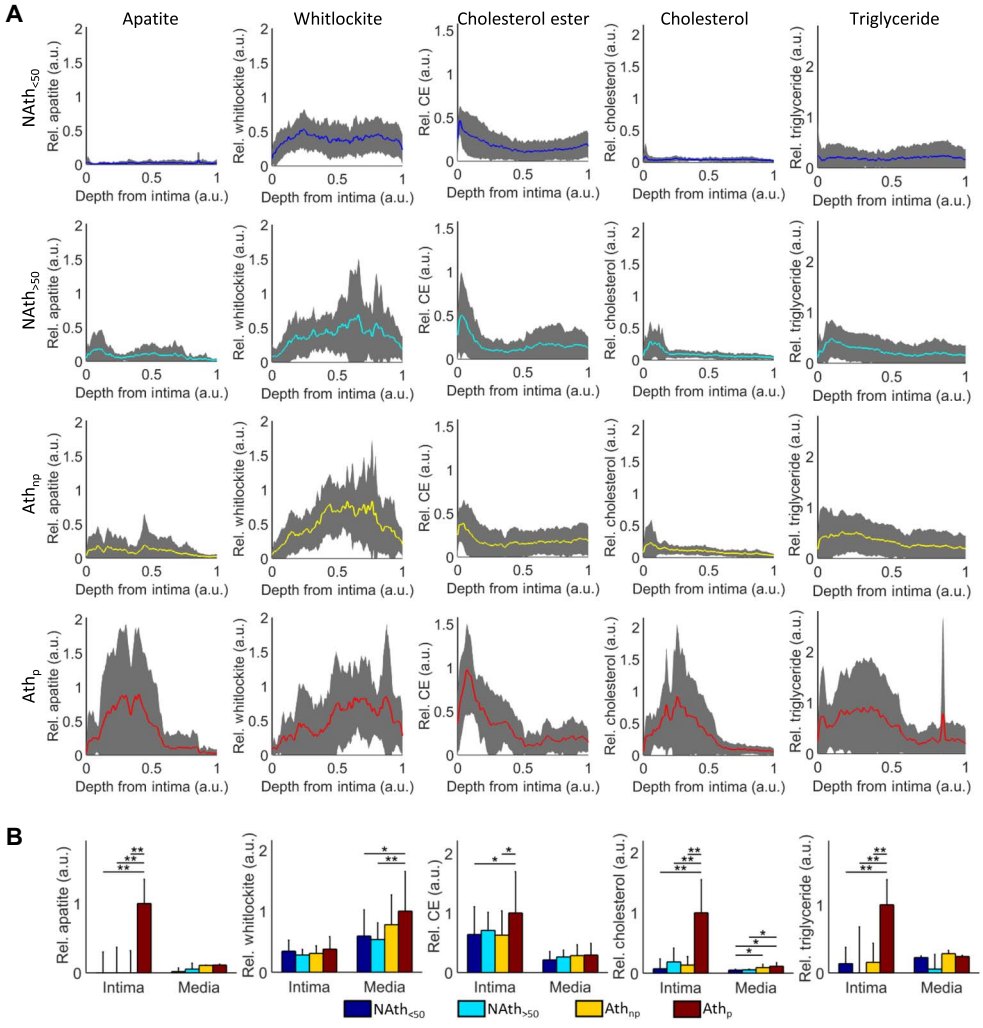

Fig. 4. Depth-dependent profiles of the major components in aortic intima and media based on VCA results, normalized to the maximum for each component. (**A**) The relative concentration (Rel.) was summed along the normalized depth of the aorta from the surface of the intima; 0, assigned to the media-adventitia interface; 1, plotted with ±1 SD. (**B**) Averages of the relative concentrations within the intima and media, normalized to area of the Raman images; error bars denote 95% confidence intervals. Statistical significance was defined using GLM regression followed by ANOVA. CE, cholesterol ester. $^{*}P < 0.05$, $^{**}P < 0.01$, $n \geq 9$ donors per group. a.u., arbitrary units.

spectrometry studies comparing cholesterol to the fatty acid content of the plaque/intima (*59*, *60*). Increases in intracellular cholesterol and cholesterol ester in the aortic media directly underlying a plaque have also been previously reported (*61*).

Another component of the aorta observed in this study is triglycerides. Hypertriglyceridemia is a prevalent risk factor for atherosclerosis (*62*). Although triglycerides are usually found in the adventitia (*63*), our study revealed that very low levels of triglycerides are present in the intima and media of all experimental groups (fig. S4). We also identified a significant increase in relative levels of triglycerides in the plaque of the atherosclerotic plaque group compared to nonatherosclerotic groups. This observation is in disagreement with a previous scanning densitometry study that showed no difference in triglyceride levels with tissue digestion (*61*). This discrepancy may be due to an inaccuracy of the lipid identification method or the extensive multistep digestion process.

Macrophage immunofluorescence also increased in atherosclerotic plaques and in the aortic media of atherosclerotic and nonatherosclerotic tissues with age. Macrophage presence in the plaque and adventitia of atherosclerotic tissues has been reported in previous literatures (*64*–*67*). In the nonatherosclerotic aortic wall of donors above 65 years of age, macrophages have been reported to be sporadically present even in the absence of lipids (*68*). This concurrent increase and similar depth profile of macrophage, apatite, triglyceride, and cholesterol in atherosclerotic plaques and the increase in apatite in the directly underlying media suggest a local and complex interplay of mechanisms that could involve macrophages. However, further studies are needed to confirm the relationship.

Intimal reduction of β-carotene in atherosclerosis

Here, we found that the intima/plaque areas of both atherosclerotic experimental groups presented significantly lower relative content of β-carotene compared to the nonatherosclerotic group below 50 years of age. Carotenoids, which are strong Raman scatterers, are antioxidants with potentially protective effects against atherosclerotic plaques (*69*–*71*). Therefore, it is interesting to consider that the levels of β-carotene, an antioxidant, are decreased not only in atherosclerotic plaques but also in the intima away from the lesion compared to healthy tissue. Although β-carotene bioavailability in humans is mainly through diet, it remains unclear whether dietary differences or changes in the tissue that affect

accumulation are responsible for this finding. Studies of β-carotene supplementation and those of the relationship between β-carotene serum levels and atherosclerosis have thus far been proven contradictory or inconclusive (*72*).

Mechanistic implications

Changes in the biochemical contents of atherosclerotic aortic tissues compared to aortic media were found to be both global and localized to the atherosclerotic plaque. A localized increase in mineral in the aortic media suggests that atherosclerotic lesions are not only confined to the plaque itself but also extend into the aortic media. Thus, we affirm that atherosclerosis is an aggravator of the aortic medial calcification. The difference in the mineral population in medial calcification in conjunction with atherosclerosis suggests a distinct mechanism compared to medial calcification in aging.

Limitations

The relative quantification of nine major components of human aortic tissues using Raman spectroscopy combined with the VCA analysis provided important insights into the makeup of healthy versus diseased aortic tissues and the impact of aging. It is important to highlight the limitations associated with this approach to aid in the interpretation of results. Because it was not possible to include all biochemicals present in the aorta in the least-squares regression, there is a certain degree of lack of fit. This was exacerbated by the coexistence of diverse components that included minerals, proteins, and lipids. Further, the different abilities of compounds to scatter light may be misleading if not taken into account. For example, β-carotene and minerals are strong Raman scatterers. Thus, the quantities of these compounds should not be compared relative to each other.

Despite these limitations, we have unearthed significant new insights into the characterization of aortic tissue through the use of Raman spectroscopy. The major extracellular matrix macromolecules of the aorta, elastin, and collagen are identified, in addition to the two mineral phases, different lipid types, actin (a major cytoskeletal molecule of contractile smooth muscle cells), and β-carotene. Together, the results of this study open new avenues that could lead to an improved understanding of cardiovascular biology and pathology and potentially contribute to the development of novel therapeutic approaches for the treatment of cardiovascular disease.

CONCLUSIONS

Here, we showed for the first time that Raman spectroscopy can be used to quantify the spatial distribution of not only specific proteins and lipids but also the specific mineral species across aortic tissue cross sections. We delineated differences in aortic tissue composition due to atherosclerosis and aging and found indications of increased medial calcification in atherosclerosis. Our results indicate that this exacerbation of calcification may be via a distinct mechanism at play than that during normal aging. The observed changes in atherosclerotic tissues compared to nonatherosclerotic tissues contribute to the knowledge of the field of cardiovascular calcification.

MATERIALS AND METHODS

Experimental design

This study quantitatively characterized full cross sections of atherosclerotic and healthy human aortic tissues using Raman spectroscopy imaging and multivariate analysis. Raman spectroscopy imaging of human aortic tissues (from atherosclerotic donors above 50 years of age) was performed on sites at and away from atherosclerotic plaque regions. Human aortic tissues from nonatherosclerotic donors above and below 50 years or age were also characterized using Raman spectroscopy imaging. The images were then further processed and analyzed by VCA.

Aorta sample preparation

Human thoracic aorta tissue specimens (n = 41) were obtained from tissue donors (n = 31) that had been rejected for use as homografts because of the presence of atheroma (Ath_{np} and Ath_{p}) or were microinfected ($NAth_{<50}$ and $NAth_{>50}$). The samples were supplied by the Oxford Heart Valve Bank at John Radcliffe Hospital, Oxford. Tissue samples were kept at −80°C. Ethical approval for this work has been obtained from the Health Research Authority–National Research Ethics Service (NRES) Committee London-Stanmore (reference #10/H0724/18) for use of human valve and cardiac tissue from heart valve donors and patients undergoing valve replacement surgery. These tissues include portions of the thoracic aorta.

One to two samples from each frozen specimen were excised. Samples spanned the entire cross section and had an area of approximately 10 mm × 10 mm. The samples were thawed and fixed in 4% (w/v) formaldehyde (≥36.0%, BioReagent; Sigma-Aldrich) in a phosphate-buffered saline solution (PBS; Gibco) overnight at 4°C. Next, the samples were cut across the cross section in a cryostat (Bright Instruments Co.) at −20°C to achieve a smooth surface for Raman spectroscopy imaging.

Pure reference biochemicals

A reference library of biochemicals was measured for comparison with the Raman spectral signatures obtained from the tissues. All reference Raman spectra were measured using a WITec alpha300 R+ confocal Raman microscope system with a 785-nm laser. A Zeiss EC Epiplan 50×/0.75 HD objective was used. Commercially available powders (Sigma-Aldrich) were used as pure reference. The powders measured were as follows: collagen from chicken sternal cartilage, elastin from bovine neck ligament, actin from bovine muscle, β-carotene, cholesterol, cholesteryl linoleate, and synthetic hydroxyapatite. Pure triglyceride mix in liquid form (Sigma-Aldrich) was also measured. To achieve a high signal-to-noise ratio, all spectra were acquired with an integration time of 15 s.

Raman spectroscopic imaging

All spectra from the aorta samples were measured while immersed in PBS. The WITec alpha300 R+ confocal Raman microscope system with a 785-nm laser was used to collect the spectra. The high confocality of this system ensured that highly resolved biochemical components could be resolved following spectral unmixing. The spectral resolution of the spectrometer was 9 cm^{-1}. Raman images of 200 μm × 200 μm with a step size of 0.8 μm × 0.8 μm were acquired with a Zeiss W Plan-Apochromat 63×/1.0 objective, with 1-s integration time, under a laser power of 100 mW at objective. Sample degradation was not observed using this laser power. Full cross-sectional images with a step size of 3 μm × 3 μm were acquired with a Zeiss W N-Achroplan 10×/0.3 objective, with 1-s integration time. The Raman spectra were corrected for the instrument response of the system using a traceable Raman standard (STM-2245, National Institute of Standards and Technology).

Univariate analysis and quantification

The raw Raman spectra were baseline-corrected with a third-order polynomial curve using the Project FOUR software (version 4.0, WITec) and normalized to the area under the curve on Matlab. Univariate intensity heat maps were plotted on the Project FOUR software using a sum filter with background subtraction. Cosmic rays were found by calculating the second derivative of each spectrum. The brightness and contrast of the images have been adjusted to improve visual clarity.

Univariate area quantification (ratios) of mineral phases in the tissue was calculated by counting the number of spectra containing the mineral peak at 960 cm^{-1} for apatite and 970 cm^{-1} for whitlockite. The ratio was calculated by taking the sums of apatite-containing spectra over the sums of all mineral-containing spectra.

Multivariate analysis and quantification

Multivariate analysis of the Raman spectroscopic data was performed on a Linux Ubuntu v15.04 multicore server (12 core, i7 3.3-GHz processors, and 64-gigabyte memory) on Matlab version R2015a (MathWorks), unless stated otherwise. The raw Raman spectra were baseline-corrected with a third-order polynomial curve using the Project FOUR software (version 4.0, WITec) and then normalized to the area under the curve on Matlab, which reduced signal intensity variability and enabled comparisons between different images.

The unmixing algorithm VCA was then applied to the Raman imaging data set using techniques previously described (*73*). Spectral unmixing was used to reduce the dimensionality of the data into nine pure components called endmembers. Each of these endmembers represented pixels with a very high concentration of one specific biochemical component. The number of endmembers was chosen on the basis of supervised analysis and correlation with the pure biochemical reference database. Nonnegative least-squares curve fitting was then performed on each spectrum in the data set against the VCA endmembers. This yielded the relative contributions of each endmember for each spectrum. The nonnegative least-squares regression was computed for each spectrum relative to the selected VCA endmembers to generate Raman signal contribution values of each component represented by each endmember. To ensure that the endmember provided meaningful biochemical information, we calculated the R^2 with the respective laboratory-grade reference biochemical measured. All depth profile graphs were depth-normalized for each map, with 0 assigned as the edge between the aortic wall and the lumen and 1 assigned as the border between the media and the adventitia of the aorta, which was denoted by a high collagen content (*74*, *75*).

Cryosection

Following Raman spectroscopy imaging, the representative aorta samples were embedded in Tissue-Tek O.C.T. (optimum cutting temperature) compound (Sakura Finetek) and frozen in liquid nitrogen–cooled isopentane. Tissue sections were cut to 10 μm with a cryostat (Bright Instruments Co.) set at −20°C. The sections were air-dried at room temperature overnight and then kept at −20°C. The frozen sections were rehydrated in PBS before staining.

Histology

Alizarin red S, a histologic stain for calcium and magnesium (Sigma-Aldrich), was used at pH 4.5 for 2 min. Picrosirius red, a histologic stain for fibrillar collagen, was applied for 1 hour. Verhoeff trichrome stained the elastin and nuclei (black), smooth muscle cytoplasm (red), and collagen (blue). Verhoeff trichrome was carried out using Elastic Stain Kit (Abcam) and Masson's Trichrome Stain Kit (Polysciences) (*76*). The slides were mounted with Histomount (National Diagnostics). Nile red, a fluorescent lipophilic dye (Sigma-Aldrich), was used at 1 μg/ml in PBS, diluted from a dimethyl sulfoxide stock solution (1 mg/ml), and applied for 10 min. The slides were mounted with Vectashield Mounting Medium with the fluorescent nuclear stain DAPI (Vector Laboratories).

Immunofluorescence

Cryosections were permeated with 0.2% (v/v) Triton X-100 (Sigma-Aldrich) in PBS for 15 min, washed with PBS, and then treated with TrueBlack (Biotium) for 30 s. The slides were blocked in 10% (v/v) donkey serum (VWR International), 5% (w/v) bovine serum albumin (Sigma-Aldrich), and 0.3 M glycine (Sigma-Aldrich) for 1 hour. Samples were stained with 1:50 anti-CD68 (Abcam) and 1:100 anti–α-SMA (Abcam) overnight at 4°C in PBS. The samples were washed extensively with PBS before incubating with 1:400 donkey anti-mouse immunoglobulin G (IgG) (H + L) (Thermo Fisher Scientific) and donkey anti-goat IgG (H + L) (Thermo Fisher Scientific) in PBS for 1 hour. Nuclei were stained with 1:500 DAPI (Thermo Fisher Scientific) in PBS for 1 min. The samples were mounted with Fluoromount Aqueous Mounting Medium (Sigma-Aldrich).

Microscopy

The histology and immunofluorescence slides were imaged using an inverted Zeiss Axio Observer microscope (20×/0.4 objective) with bright-field and fluorescence channels. Images were stitched using the ZEN software (Zeiss Microscopy), and the white balance for the background was adjusted using Fiji.

Statistical analysis

Statistical analysis was performed on Matlab. Depth normalization was performed by interpolating the matrix of abundances for each component with cubic interpolation. The means and SDs were calculated for each point across the normalized depth. For bar graph comparison between experimental groups, Raman signal contribution values from the VCA analysis were analyzed using ordinary least-squares regression based on GLMs in the statistical software R, using the rms package. The rate of change of various Raman spectral components based on VCA endmembers was modeled as the dependent variable, and regression coefficients were calculated for independent variables of pathological grouping and patient descriptors. To make comparisons because these independent variables changed with disease presentation, generalized estimating equations were used (as previously described) to enable clustering of measurements obtained from a single specimen (*77*–*79*). The generated regression curves for different pathologies were compared. Specifically for this analysis, the relative concentrations of interest were the age, gender, and presence/proximity to atherosclerotic plaques (categorical). These patient descriptors were included as independent variables. Heteroscedasticity in the data set was addressed by using the robust covariance function created in the rms package ("robcov") to adjust the standard errors. Finally, to look at interactions between specific disease and patient variables, an ANOVA was performed on the generated GLM regression curves from the developed regression model, which were represented with *P* values. For comparison between the intima and the media and for comparison within the individual representative donor, because of nonnormal distribution as measured by a Lilliefors test, *P* values were calculated by the nonparametric Wilcoxon rank sum test.

SUPPLEMENTARY MATERIALS

Supplementary material for this article is available at http://advances.sciencemag.org/cgi/content/full/3/12/e1701156/DC1

fig. S1. Comparison of the relative concentrations of apatite and whitlockite between the aortic intima and the media.

fig. S2. VCA on Raman spectroscopy images and relevant histology images.

fig. S3. Raman spectra of pure commercial powders.

fig. S4. Depth-dependent profiles of β-carotene, elastin, collagen, and actin in the aortic intima and media based on VCA results, normalized to the maximum for each component.

fig. S5. Representative comparison within one donor, for the relative concentrations of major components within the aortic intima and media.

REFERENCES AND NOTES

1. S. Mendis, P. Puska, B. Norrving, *Global Atlas on Cardiovascular Disease Prevention and Control* (World Health Organization, 2011), pp. 2–14.
2. J. A. Finegold, P. Asaria, D. P. Francis, Mortality from ischaemic heart disease by country, region, and age: Statistics from World Health Organisation and United Nations. *Int. J. Cardiol.* **168**, 934–945 (2013).
3. N. Townsend, M. Nichols, P. Scarborough, M. Rayner, Cardiovascular disease in Europe—Epidemiological update 2015. *Eur. Heart J.* **36**, 2696–2705 (2015).
4. R. C. Johnson, J. A. Leopold, J. Loscalzo, Vascular calcification: Pathobiological mechanisms and clinical implications. *Circ. Res.* **99**, 1044–1059 (2006).
5. L. L. Demer, Y. Tintut, Vascular calcification: Pathobiology of a multifaceted disease. *Circulation* **117**, 2938–2948 (2008).
6. P. Lanzer, M. Boehm, V. Sorribas, M. Thiriet, J. Janzen, T. Zeller, C. St. Hilaire, C. Shanahan, Medial vascular calcification revisited: Review and perspectives. *Eur. Heart J.* **35**, 1515–1525 (2014).
7. M. R. Davies, K. A. Hruska, Pathophysiological mechanisms of vascular calcification in end-stage renal disease. *Kidney Int.* **60**, 472–479 (2001).
8. J. D. Hutcheson, N. Maldonado, E. Aikawa, Small entities with large impact: Microcalcifications and atherosclerotic plaque vulnerability. *Curr. Opin. Lipidol.* **25**, 327–332 (2014).
9. E. Aikawa, M. Nahrendorf, J.-L. Figueiredo, F. K. Swirski, T. Shtatland, R. H. Kohler, F. A. Jaffer, M. Aikawa, R. Weissleder, Osteogenesis associates with inflammation in early-stage atherosclerosis evaluated by molecular imaging in vivo. *Circulation* **116**, 2841–2850 (2007).
10. G. Wick, C. Grundtman, *Inflammation and Atherosclerosis* (Springer Science & Business Media, 2011).
11. J. D. Reid, M. E. Andersen, Medial calcification (whitlockite) in the aorta. *Atherosclerosis* **101**, 213–224 (1993).
12. R. J. Elliott, L. T. McGrath, Calcification of the human thoracic aorta during aging. *Calcif. Tissue Int.* **54**, 268–273 (1994).
13. Y. Tohno, S. Tohno, T. Minami, M. Ichii, Y. Okazaki, M. Utsumi, F. Nishiwaki, Y. Moriwake, M.-O. Yamada, T. Araki, Age-related change of mineral content in the human thoracic aorta and in the human cerebral artery. *Biol. Trace Elem. Res.* **54**, 23–31 (1996).
14. S. Bertazzo, E. Gentleman, K. L. Cloyd, A. H. Chester, M. H. Yacoub, M. M. Stevens, Nano-analytical electron microscopy reveals fundamental insights into human cardiovascular tissue calcification. *Nat. Mater.* **12**, 576–583 (2013).
15. R. Villa-Bellosta, A. Millan, V. Sorribas, Role of calcium-phosphate deposition in vascular smooth muscle cell calcification. *Am. J. Physiol. Cell Physiol.* **300**, C210–C220 (2011).
16. L. Hortells, C. Sosa, Á. Millán, V. Sorribas, Critical parameters of the in vitro method of vascular smooth muscle cell calcification. *PLOS ONE* **10**, e0141751 (2015).
17. W. Mohr, E. Görz, Granuläre mediakalzinose der aorta. Strukturelle befunde, historischer Rückblick und pathogenetische bedeutung. *Z. Kardiol.* **90**, 916–928 (2001).
18. G. Pugliese, C. Iacobini, C. B. Fantauzzi, S. Menini, The dark and bright side of atherosclerotic calcification. *Atherosclerosis* **238**, 220–230 (2015).
19. S. E. P. New, C. Goettsch, M. Aikawa, J. F. Marchini, M. Shibasaki, K. Yabusaki, P. Libby, C. M. Shanahan, K. Croce, E. Aikawa, Macrophage-derived matrix vesicles: An alternative novel mechanism for microcalcification in atherosclerotic plaques. *Circ. Res.* **113**, 72–77 (2013).
20. H. C. Stary, A. B. Chandler, R. E. Dinsmore, V. Fuster, S. Glagov, W. Insull, M. E. Rosenfeld, C. J. Schwartz, W. D. Wagner, R. W. Wissler, A definition of advanced types of atherosclerotic lesions and a histological classification of atherosclerosis. A report from the Committee on Vascular Lesions of the Council on Arteriosclerosis, American Heart Association. *Circulation* **92**, 1355–1374 (1995).
21. G. K. Hansson, Inflammation, atherosclerosis, and coronary artery disease. *N. Engl. J. Med.* **352**, 1685–1695 (2005).
22. R. Stocker, J. F. Keaney Jr., Role of oxidative modifications in atherosclerosis. *Physiol. Rev.* **84**, 1381–1478 (2004).
23. R. Ross, Atherosclerosis—An inflammatory disease. *N. Engl. J. Med.* **340**, 115–126 (1999).
24. R. Ross, The pathogenesis of atherosclerosis: A perspective for the 1990s. *Nature* **362**, 801–809 (1993).
25. E. M. Green, J. C. Mansfield, J. S. Bell, C. P. Winlove, The structure and micromechanics of elastic tissue. *Interface Focus* **4**, 20130058 (2014).
26. N. Sakata, A. Noma, Y. Yamamoto, K. Okamoto, J. Meng, S. Takebayashi, R. Nagai, S. Horiuchi, Modification of elastin by pentosidine is associated with the calcification of aortic media in patients with end-stage renal disease. *Nephrol. Dial. Transplant.* **18**, 1601–1609 (2003).
27. E. Schiffmann, G. R. Martin, E. J. Miller, Matrices that calcify, in *Biological Calcification: Cellular and Molecular Aspects*, H. Schraer, Ed. (Springer, 1970), pp. 27–67.
28. N. Niederhoffer, I. Lartaud-Idjouadiene, P. Giummelly, C. Duvivier, R. Peslin, J. Atkinson, Calcification of medial elastic fibers and aortic elasticity. *Hypertension* **29**, 999–1006 (1997).
29. M. E. Edmonds, Medial arterial calcification and diabetes mellitus. *Z. Kardiol.* **89**, S101–S104 (2000).
30. L. Park, K. G. Raman, K. J. Lee, Y. Lu, L. J. Ferran Jr., W. S. Chow, D. Stern, A. M. Schmidt, Suppression of accelerated diabetic atherosclerosis by the soluble receptor for advanced glycation endproducts. *Nat. Med.* **4**, 1025–1031 (1998).
31. L. G. Bucciarelli, T. Wendt, W. Qu, Y. Lu, E. Lalla, L. L. Rong, M. T. Goova, B. Moser, T. Kislinger, D. C. Lee, Y. Kashyap, D. M. Stern, A. M. Schmidt, RAGE blockade stabilizes established atherosclerosis in diabetic apolipoprotein E–null mice. *Circulation* **106**, 2827–2835 (2002).
32. A. Tanimura, D. H. McGregor, H. C. Anderson, Matrix vesicles in atherosclerotic calcification. *Proc. Soc. Exp. Biol. Med.* **172**, 173–177 (1983).
33. M. A. B. Hedegaard, K. L. Cloyd, C.-M. Horejs, M. M. Stevens, Model based variable selection as a tool to highlight biological differences in Raman spectra of cells. *Analyst* **139**, 4629–4633 (2014).
34. M. S. Bergholt, J.-P. St-Pierre, G. S. Offeddu, P. A. Parmar, M. B. Albro, J. L. Puetzer, M. L. Oyen, M. M. Stevens, Raman spectroscopy reveals new insights into the zonal organization of native and tissue-engineered articular cartilage. *ACS Cent. Sci.* **2**, 885–895 (2016).
35. M. A. B. Hedegaard, M. S. Bergholt, M. M. Stevens, Quantitative multi-image analysis for biomedical Raman spectroscopic imaging. *J. Biophotonics* **9**, 542–550 (2016).
36. H. P. Buschman, G. Deinum, J. T. Motz, M. Fitzmaurice, J. R. Kramer, A. van der Laarse, A. V. Bruschke, M. S. Feld, Raman microspectroscopy of human coronary atherosclerosis: Biochemical assessment of cellular and extracellular morphologic structures in situ. *Cardiovasc. Pathol.* **10**, 69–82 (2001).
37. H. P. Buschman, J. T. Motz, G. Deinum, T. J. Römer, M. Fitzmaurice, J. R. Kramer, A. van der Laarse, A. V. Bruschke, M. S. Feld, Diagnosis of human coronary atherosclerosis by morphology-based Raman spectroscopy. *Cardiovasc. Pathol.* **10**, 59–68 (2001).
38. A. S. Haka, J. R. Kramer, R. R. Dasari, M. Fitzmaurice, Mechanism of ceroid formation in atherosclerotic plaque: In situ studies using a combination of Raman and fluorescence spectroscopy. *J. Biomed. Opt.* **16**, 011011 (2011).
39. S.-H. Kim, E.-S. Lee, J. Y. Lee, E. S. Lee, B.-S. Lee, J. E. Park, D. W. Moon, Multiplex coherent anti-stokes Raman spectroscopy images intact atheromatous lesions and concomitantly identifies distinct chemical profiles of atherosclerotic lipids. *Circ. Res.* **106**, 1332–1341 (2010).
40. M. Pilarczyk, A. Rygula, A. Kaczor, L. Mateuszuk, E. Maślak, S. Chlopicki, M. Baranska, A novel approach to investigate vascular wall in 3D: Combined Raman spectroscopy and atomic force microscopy for aorta *en face* imaging. *Vib. Spectrosc.* **75**, 39–44 (2014).
41. M. Pilarczyk, L. Mateuszuk, A. Rygula, M. Kepczynski, S. Chlopicki, M. Baranska, A. Kaczor, Endothelium in spots—High-content imaging of lipid rafts clusters in db/db mice. *PLOS ONE* **9**, e106065 (2014).
42. C. Matthäus, S. Dochow, G. Bergner, A. Lattermann, B. F. M. Romeike, E. T. Marple, C. Krafft, B. Dietzek, B. R. Brehm, J. Popp, In vivo characterization of atherosclerotic plaque depositions by Raman-probe spectroscopy and in vitro coherent anti-stokes Raman scattering microscopic imaging on a rabbit model. *Anal. Chem.* **84**, 7845–7851 (2012).
43. S. W. E. van de Poll, K. Kastelijn, T. C. Bakker Schut, C. Strijder, G. Pasterkamp, G. J. Puppels, A. van der Laarse, On-line detection of cholesterol and calcification by catheter based Raman spectroscopy in human atherosclerotic plaque ex vivo. *Heart* **89**, 1078–1082 (2003).
44. D. D. Klug, D. L. Singleton, V. M. Walley, Laser Raman spectrum of calcified human aorta. *Lasers Surg. Med.* **12**, 13–17 (1992).
45. R. Manoharan, J. J. Baraga, M. S. Feld, R. P. Rava, Quantitative histochemical analysis of human artery using Raman spectroscopy. *J. Photochem. Photobiol. B Biol.* **16**, 211–233 (1992).
46. K. Czamara, J. Natorska, P. Kapusta, M. Baranska, A. Kaczor, Raman microspectroscopy of human aortic valves: Investigation of the local and global biochemical changes associated with calcification in aortic stenosis. *Analyst* **140**, 2164–2170 (2015).
47. A. Lattermann, C. Matthäus, N. Bergner, C. Beleites, B. F. Romeike, C. Krafft, B. R. Brehm, J. Popp, Characterization of atherosclerotic plaque depositions by Raman and FTIR imaging. *J. Biophotonics* **6**, 110–121 (2013).

48. Z. Movasaghi, S. Rehman, I. U. Rehman, Raman spectroscopy of biological tissues. *Appl. Spectrosc. Rev.* **42**, 493–541 (2007).
49. B. G. Frushour, J. L. Koenig, Raman scattering of collagen, gelatin, and elastin. *Biopolymers* **14**, 379–391 (1975).
50. L. Popović, D. de Waal, J. C. A. Boeyens, Correlation between Raman wavenumbers and P–O bond lengths in crystalline inorganic phosphates. *J. Raman Spectrosc.* **36**, 2–11 (2005).
51. B. L. Jolliff, J. J. Freeman, B. Wopenka, Structural comparison of lunar, terrestrial, and synthetic whitlockite using laser Raman microprobe spectroscopy. *Lunar Planet. Sci.* **27**, 613–614 (1996).
52. C. Xu, K. Karan, X. Yao, Y. Wang, Molecular structural analysis of noncarious cervical sclerotic dentin using Raman spectroscopy. *J. Raman Spectrosc.* **40**, 1780–1785 (2009).
53. S. Sarig, T. A. Weiss, I. Katz, F. Kahana, R. Azoury, E. Okon, H. S. Kruth, Detection of cholesterol associated with calcium mineral using confocal fluorescence microscopy. *Lab. Invest.* **71**, 782–787 (1994).
54. M. Shiomi, S. Yamada, A. Matsukawa, H. Itabe, T. Ito, Invasion of atheromatous plaques into tunica media causes coronary outward remodeling in WHHLMI rabbits. *Atherosclerosis* **198**, 287–293 (2008).
55. G. Steiner, Diabetes and atherosclerosis: An overview. *Diabetes* **30** (suppl. 2), 1–7 (1981).
56. J. Stamler, O. Vaccaro, J. D. Neaton, D. Wentworth; Multiple Risk Factor Intervention Trial Research Group, Diabetes, other risk factors, and 12-yr cardiovascular mortality for men screened in the Multiple Risk Factor Intervention Trial. *Diabetes Care* **16**, 434–444 (1993).
57. S. Lehto, L. Niskanen, M. Suhonen, T. Rönnemaa, M. Laakso, Medial artery calcification. A neglected harbinger of cardiovascular complications in non–insulin-dependent diabetes mellitus. *Arterioscler. Thromb. Vasc. Biol.* **16**, 978–983 (1996).
58. J. E. Everhart, D. J. Pettitt, W. C. Knowler, F. A. Rose, P. H. Bennett, Medial arterial calcification and its association with mortality and complications of diabetes. *Diabetologia* **31**, 16–23 (1988).
59. K. L. H. Carpenter, S. E. Taylor, C. van der Veen, B. K. Williamson, J. A. Ballantine, M. J. Mitchinson, Lipids and oxidised lipids in human atherosclerotic lesions at different stages of development. *Biochim. Biophys. Acta* **1256**, 141–150 (1995).
60. K. L. H. Carpenter, S. E. Taylor, J. A. Ballantine, B. Fussell, B. Halliwell, M. J. Mitchinson, Lipids and oxidised lipids in human atheroma and normal aorta. *Biochim. Biophys. Acta* **1167**, 121–130 (1993).
61. A. N. Orekhov, V. V. Tertov, I. D. Novikov, A. V. Krushinsky, E. R. Andreeva, V. Z. Lankin, V. N. Smirnov, Lipids in cells of atherosclerotic and uninvolved human aorta: I. Lipid composition of aortic tissue and enzyme-isolated and cultured cells. *Exp. Mol. Pathol.* **42**, 117–137 (1985).
62. R. S. Rosenson, M. H. Davidson, B. J. Hirsh, S. Kathiresan, D. Gaudet, Genetics and causality of triglyceride-rich lipoproteins in atherosclerotic cardiovascular disease. *J. Am. Coll. Cardiol.* **64**, 2525–2540 (2014).
63. T. J. Römer, J. F. Brennan III, M. Fitzmaurice, M. L. Feldstein, G. Deinum, J. L. Myles, J. R. Kramer, R. S. Lees, M. S. Feld, Histopathology of human coronary atherosclerosis by quantifying its chemical composition with Raman spectroscopy. *Circulation* **97**, 878–885 (1998).
64. M. A. Houtkamp, O. J. de Boer, C. M. van der Loos, A. C. van der Wal, A. E. Becker, Adventitial infiltrates associated with advanced atherosclerotic plaques: Structural organization suggests generation of local humoral immune responses. *J. Pathol.* **193**, 263–269 (2001).
65. M. Watanabe, A. Sangawa, Y. Sasaki, M. Yamashita, M. Tanaka-Shintani, M. Shintaku, Y. Ishikawa, Distribution of inflammatory cells in adventitia changed with advancing atherosclerosis of human coronary artery. *J. Atheroscler. Thromb.* **14**, 325–331 (2007).
66. C. J. Schwartz, J. R. A. Mitchell, Cellular infiltration of the human arterial adventitia associated with atheromatous plaques. *Circulation* **26**, 73–78 (1962).
67. A. L. Ramshaw, D. V. Parums, Immunohistochemical characterization of inflammatory cells associated with advanced atherosclerosis. *Histopathology* **17**, 543–552 (1990).
68. M. Wang, J. Zhang, L.-Q. Jiang, G. Spinetti, G. Pintus, R. Monticone, F. D. Kolodgie, R. Virmani, E. G. Lakatta, Proinflammatory profile within the grossly normal aged human aortic wall. *Hypertension* **50**, 219–227 (2007).
69. A. Shaish, A. Daugherty, F. O'Sullivan, G. Schonfeld, J. W. Heinecke, Beta-carotene inhibits atherosclerosis in hypercholesterolemic rabbits. *J. Clin. Invest.* **96**, 2075–2082 (1995).
70. P. Palozza, N. I. Krinsky, Antioxidant effects of carotenoids in vivo and in vitro: An overview. *Methods Enzymol.* **213**, 403–420 (1992).
71. G.W. Burton, K. U. Ingold, beta-Carotene: An unusual type of lipid antioxidant. *Science* **224**, 569–573 (1984).
72. M. A. Gammone, G. Riccioni, N. D'Orazio, Carotenoids: Potential allies of cardiovascular health? *Food Nutr. Res.* **59**, 26762 (2015).
73. J. M. P. Nascimento, J. M. B. Dias, Vertex component analysis: A fast algorithm to unmix hyperspectral data. *IEEE Trans. Geosci. Remote Sens.* **43**, 898–910 (2005).
74. J. B. Kerr, *Functional Histology* (Mosby Elsevier, ed. 2, 2010).
75. T. J. M. Schlatmann, A. E. Becker, Histologic changes in the normal aging aorta: Implications for dissecting aortic aneurysm. *Am. J. Cardiol.* **39**, 13–20 (1977).
76. W. N. O'Connor, S. Valle, A combination Verhoeff's elastic and Masson's trichrome stain for routine histology. *Stain Technol.* **57**, 207–210 (1982).
77. C. M. O'Brien, J. L. Herington, N. Brown, I. J. Pence, B. C. Paria, J. C. Slaughter, J. Reese, A. Mahadevan-Jansen, In vivo Raman spectral analysis of impaired cervical remodeling in a mouse model of delayed parturition. *Sci. Rep.* **7**, 6835 (2017).
78. J. A. Hanley, A. Negassa, M. D. deB. Edwardes, J. E. Forrester, Statistical analysis of correlated data using generalized estimating equations: An orientation. *Am. J. Epidemiol.* **157**, 364–375 (2003).
79. S. L. Zeger, K.-Y. Liang, Longitudinal data analysis for discrete and continuous outcomes. *Biometrics* **42**, 121–130 (1986).

Acknowledgments

Funding: A.Y.F.Y., J.-P.S.-P., S.B., and M.M.S. were supported by the Rosetrees Trust and the Stoneygate Trust. W.K.-A. was supported by the British Heart Foundation Centre of Research Excellence (RE/13/4/30184). I.J.P. was supported by the Whitaker International Program, Institute of International Education, USA. M.S.B., J.-P.S.-P., and M.M.S. were funded by the grants from the UK Regenerative Medicine Platform "Acellular Approaches for Therapeutic Delivery" (MR/K026682/1) and "A Hub for Engineering and Exploiting the Stem Cell Niche" (MR/K026666/1). M.M.S. acknowledges the grant "State of the Art Biomaterials Development and Characterization of the Cell-Biomaterial Interface" (MR/L012677/1) from the MRC. M.S.B. acknowledges the support from the European Union's Horizon 2020 Research and Innovation Programme under the Marie Skłodowska-Curie Fellowship "IMAGINE" (701713). J.-P.S.-P. and M.M.S. were also supported by the Medical Engineering Solutions in the Osteoarthritis Centre of Excellence, funded by the Wellcome Trust and the Engineering and Physical Sciences Research Council (088844/Z/09/Z). J.-P.S.-P. acknowledges the Value in People Award from the Wellcome Trust Institutional Strategic Support Fund (097816/Z/11/B). M.M.S. also acknowledges the support from the European Research Council Seventh Framework Programme Consolidator grant "Naturale CG" (616417). We thank the Facility for Imaging by Light Microscopy at Imperial College London and Mr. Stephen M. Rothery.
Author contributions: A.Y.F.Y. conducted the experimental work, carried out data analysis and interpretation, and drafted the manuscript. M.S.B. advised on the experimental setup and aided with data analysis and manuscript preparation. J.-P.S.-P. and S.B. provided overall guidance on project direction and aided with study design and manuscript preparation. W.K.-A. conducted the experimental work and revised the manuscript. I.J.P. conducted statistical analysis on the data and aided with manuscript preparation. A.H.C. and M.H.Y. helped with sample procurement, aided with data interpretation, and revised the manuscript. M.M.S. supervised the study, aided with study design and data interpretation, and revised the manuscript. **Competing interests:** The authors declare that they have no competing interests. **Data and materials availability:** All data needed to evaluate the conclusions in the paper are present in the paper and/or the Supplementary Materials. Raw data is available online at DOI: 10.5281/zenodo.1045174.

Submitted 11 April 2017
Accepted 9 November 2017
Published 6 December 2017
10.1126/sciadv.1701156

Citation: A. Y. F. You, M. S. Bergholt, J.-P. St-Pierre, W. Kit-Anan, I. J. Pence, A. H. Chester, M. H. Yacoub, S. Bertazzo, M. M. Stevens, Raman spectroscopy imaging reveals interplay between atherosclerosis and medial calcification in the human aorta. *Sci. Adv.* **3**, e1701156 (2017).

Science Advances

Raman spectroscopy imaging reveals interplay between atherosclerosis and medial calcification in the human aorta

Amanda Y. F. You, Mads S. Bergholt, Jean-Philippe St-Pierre, Worrapong Kit-Anan, Isaac J. Pence, Adrian H. Chester, Magdi H. Yacoub, Sergio Bertazzo and Molly M. Stevens

Sci Adv **3** (12), e1701156.
DOI: 10.1126/sciadv.1701156